Supporting Information for

Macroscopic Length Scale of Water Super-Transport in Single Ultralong Carbon Nanotube

Silei Sun[1#], Boyuan Shen[2#]*, Jun Gao[1], Zhenxing Zhu[1]*, Fei Wei[1]*

[1]Beijing Key Laboratory of Green Chemical Reaction Engineering and Technology, Department of Chemical Engineering, Tsinghua University, Beijing 100084, China.

[2]Institute of Functional Nano & Soft Materials (FUNSOM), Jiangsu Key Laboratory for Carbon-Based Functional Materials & Devices, Soochow University, Suzhou 215123, Jiangsu, China.

[#]These authors contributed equally to this work.

*Corresponding authors. Emails: byshen@suda.edu.cn (B.S.); zxing@mail.tsinghua.edu.cn (Z.Z.); wf-dce@tsinghua.edu.cn (F.W.)

Table of Contents

Supplementary Discussion 1

The ultralong CNTs were synthesized by chemical vapor deposition method, which is similar to our previously reported process[33-38]. According to the Schulz-Flory distribution[33], the quantity of ultralong CNTs will exponentially decrease with the length, as indicated in the Supplementary Figure 1. Besides, in order to obtain aligned ultralong CNTs with a lower density, a higher ratio of H_2/CH_4 was used in comparison with the conventional growth method. The as-grown ultralong CNTs, especially those longer than 10 mm, are more suitable for super-transport measurement due to lack of tube-to-tube interactions and contaminations from catalyst nanoparticles.

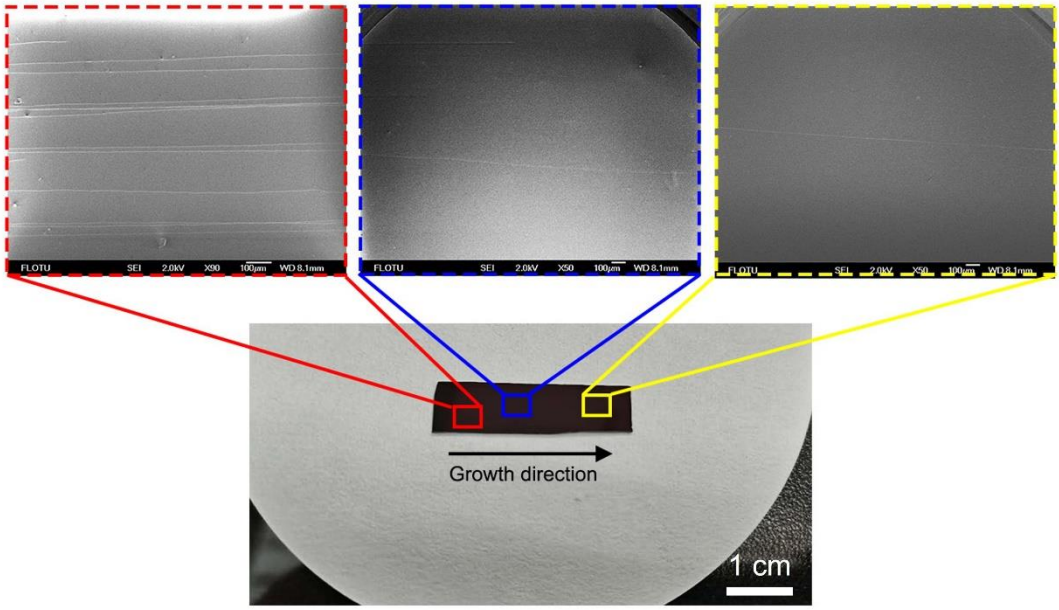

Supplementary Figure 1. The SEM images showing the ultra-lengths of these as-grown CNTs.

The ultralong CNTs can also be grown on Si/SiO_2 substrates, containing slits (300 nm deep, 5-20 μm wide) and marks fabricated by photolithography and dry etching[34]. Precise position of an individual ultralong CNT can be confirmed from the distance between the CNT and the numeric markers.

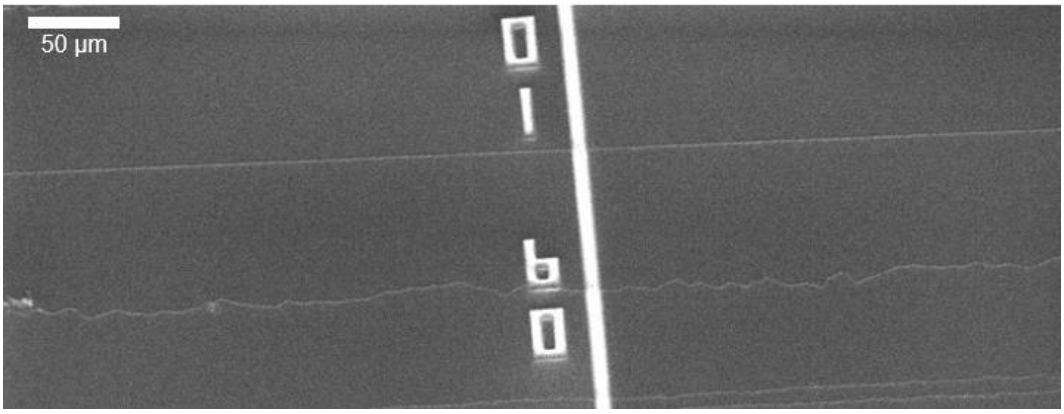

Supplementary Figure 2. The ultralong CNTs grown on the Si/SiO_2 substrate with slits and marks.

Supplementary Discussion 2

Raman spectra were collected with Horiba HR 800 equipped with a liquid-nitrogen-cooled silicon CCD detector and the excitation source at 532 nm (2.33 eV). The scattered light was collected through a 100× air objective using a backscattering configuration. Stokes Raman spectra were acquired with edge filters cutting at 100 cm^{-1}. A 600 grooves per mm grating rate was used, giving a spectral resolution better than 2 cm^{-1}. Laser power was kept at or below ~1mW to avoid the heating effect. Typical accumulation time was 60 s for each spectrum. All Raman spectra were corrected by subtracting the background signal collected at a blank slit.

Micro-Raman measurements were conducted on the suspended CNTs across the slits, manifesting their intrinsic properties with the van der Waals CNT-SiO_2 interaction being eliminated. Changes in the D-band (~1350 cm^{-1}) and G-band (~1580 cm^{-1}) Raman spectra can be used for materials characterization to probe and monitor structural modifications of the hexagonal lattice that come from the introduction of defects and the tube-to-tube interactions[44-46]. As shown in the Supplementary Figure 3, no D bands were detected on the ultralong CNTs produced from the same batch, indicating that these ultralong CNTs are defect-free with consistent diameter.

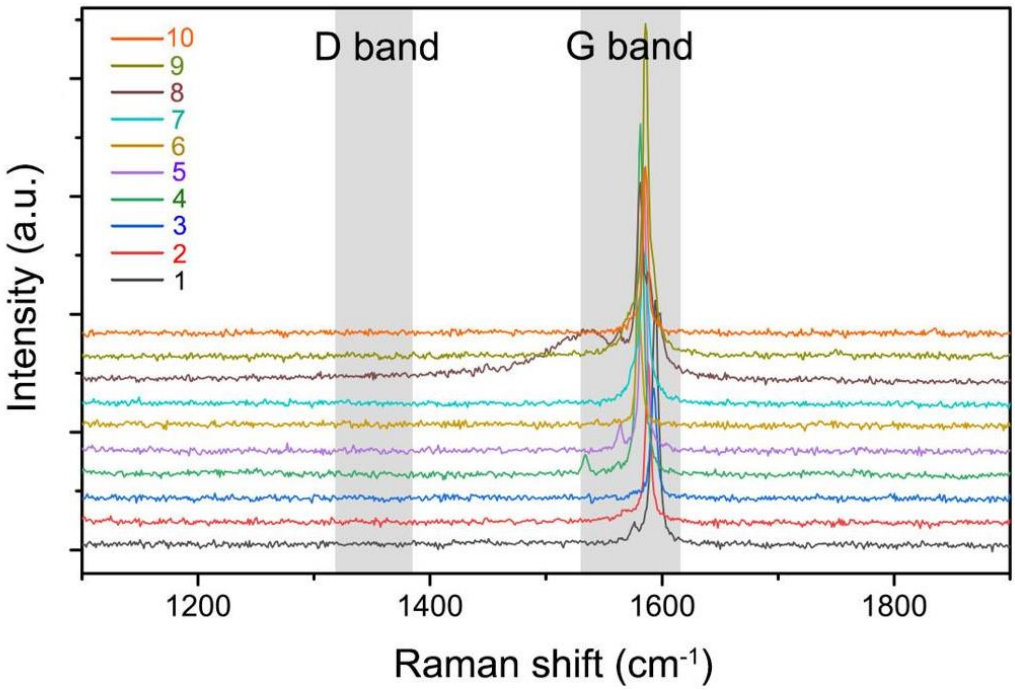

Supplementary Figure 3. The resonant Raman spectra of the ten as-grown ultralong CNTs on the same substrate.

Supplementary Discussion 3

According to the method reported in our previous work[33-38], the as-grown ultralong CNTs are mostly double walled with their diameters evenly distributed. The most accurate method to determine the diameter of a DWNT is to identify the chirality of its concentric layers. Here, we used the Raman-Rayleigh spectroscopy and electron microscopy method respectively, to identify the chirality of individual ultralong CNTs for super-transport.

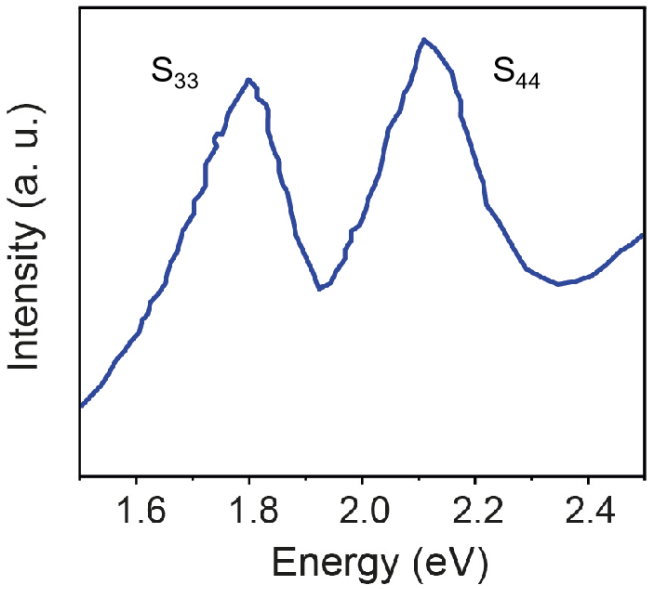

Supplementary Figure 4. The resonant Rayleigh scattering spectra of an ultralong CNT used for super-transport.

Firstly, Rayleigh scattering was greatly enhanced by the interface dipole enhancement effect[47,48], so that true-color imaging of CNTs could be achieved under an optical microscope by wide field supercontinuum laser illumination. As shown in Figure 1c, the consistent color implies the grown ultralong CNT possesses consistent chirality[49,50] and diameter without atomic defects. Then, according to the Rayleigh scattering spectrum shown in Supplementary Figure 4, we selected the laser source at 532 nm (2.33 eV) to excite the resonant Raman signal. Considering the quantum interference in DWNTs, both coupled RBM oscillations will be resonantly excited if an electronic transition of either wall matches the excitation photon energy[51]. The bimodal characteristic of the RBM mode shown in Figure 1d indicates that it is a DWNT with two excitations distributed around 198.7 cm^{-1} and 137 cm^{-1}. And the intrinsic shifts can be calculated according to the coupled oscillator model and the effective pressure variation determined by inter-tube separation, so that the chiral index (16,2)@(17,12) can be obtained from the classical Kataura plot (Supplementary Figure 5). It can be seen that the photon energies of S_{33} and S_{44} are significantly red-shifted (~-80 meV) compared with the corresponding constituent (17,12)-SWNT transitions[52], which is consistent with the electronic coupling in the incommensurate DWNTs[53].

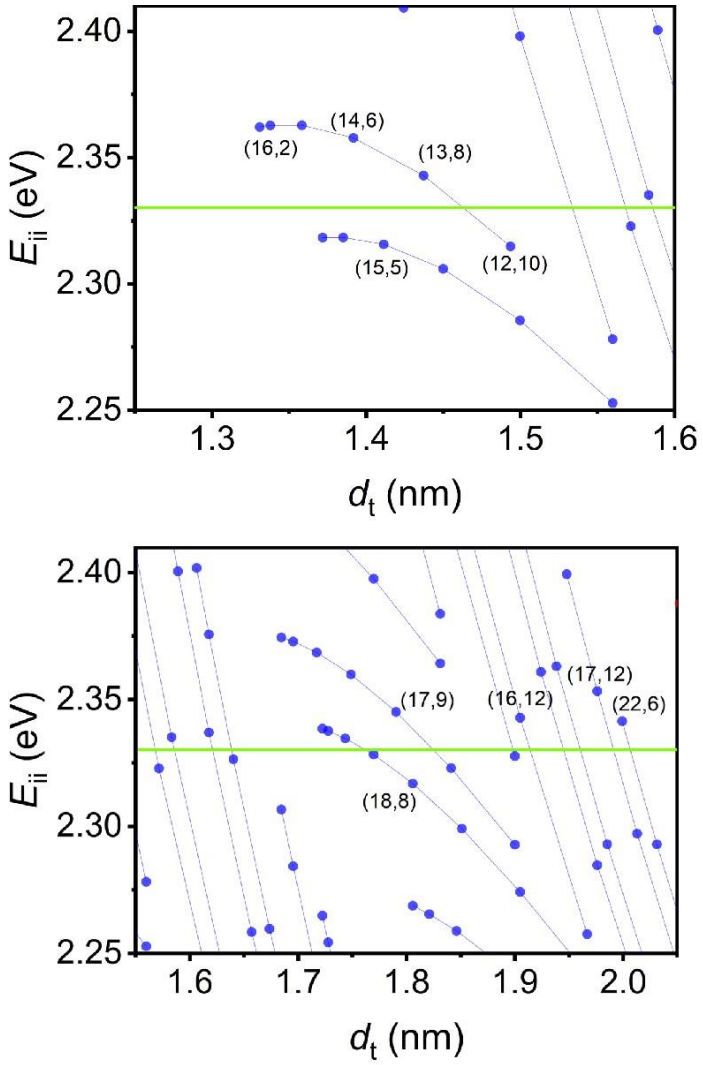

Supplementary Figure 5. Normalized Kataura plot for determining the chiral index of the inner wall (top) and outer wall (bottom) of the ultralong CNT.

Furthermore, we cut a 1.5-mm-long portion from one end of the same ultralong CNT and transferred it onto the TEM grid assisted with cellulose acetate films[54]. The cellulose acetate films were 60 μm in thickness, purchased from Beijing XXBR Tech. Co., Ltd., China. Then, TEM characterization was conducted and the results shown in the Supplementary Figure 6 clearly show that the ultralong CNT is double walled. Besides, careful electron diffraction analysis has helped to accurately identify the chiral indices of the ultralong CNT, also verifying the results deduced from the Raman-Rayleigh spectroscopy.

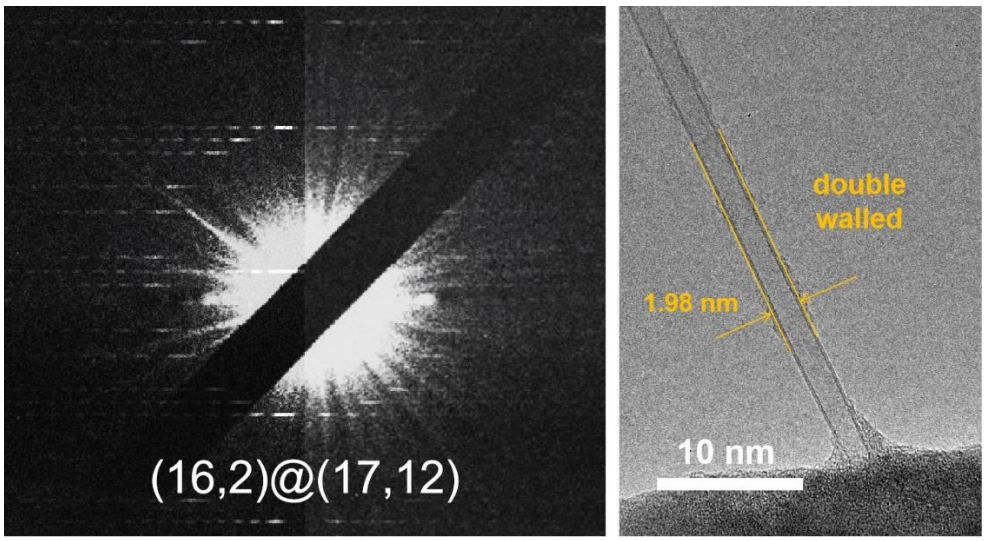

Supplementary Figure 6. Electron diffraction (left) and TEM image (right) of the ultralong CNT for super-transport.

Supplementary Discussion 4

The growth of ultralong CNT follows the kite-flying mechanism[55], where the catalyst nanoparticles maintain at the tip of the ultralong CNT, while the other end is closely attached onto the Si/SiO_2 substrate. In order to measure the water transport through an individual CNT, it is necessary to cut off both ends so that water can flow smoothly into the nanotube. Due to the strong interactions between CNTs and substrate, we used a probe (Lake Shore CRX-4K) shown in the Supplementary Figure 7 to cut off the two ends respectively of the target ultralong CNT, which was located by its distance from the numeric markers. All the operations were carried out under low temperature and vacuum conditions, in order to avoid reclosing the activated nanotube ends because of the impurity modification from the atmosphere.

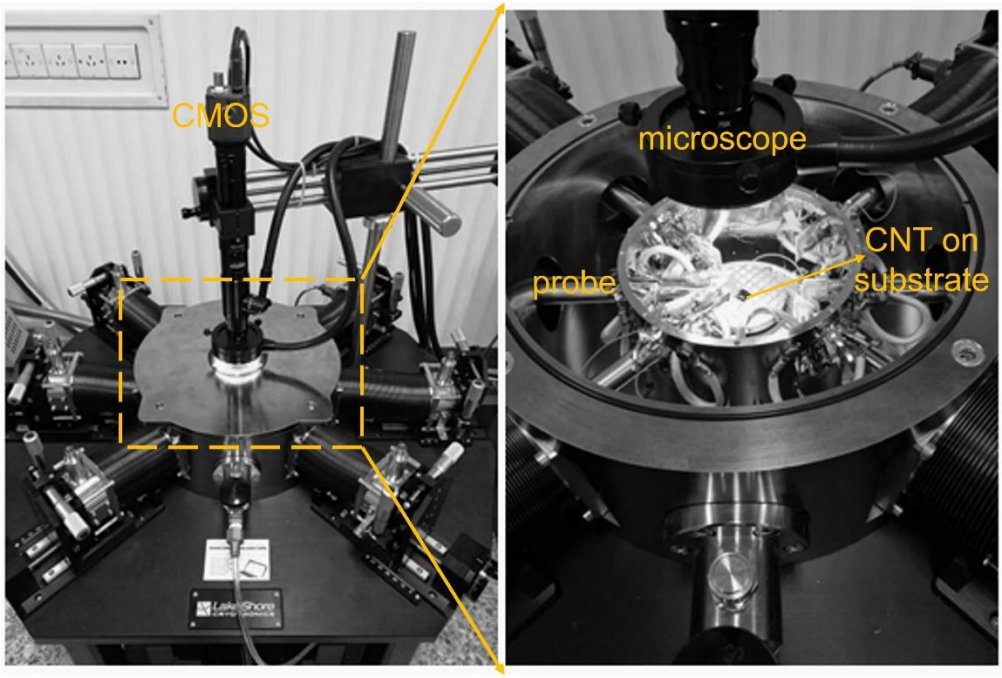

Supplementary Figure 7. Cutting off both ends of the ultralong CNT with the probe.

The same ultralong CNT before and after being cut can be seen in the SEM images of Supplementary Figure 8. As shown, the ultralong CNT maintains its original morphology despite of negligible bending near the cut-off point, which indicates that the cutting operation has no influence on the CNT. Besides, when many ultralong CNTs are horizontally aligned on the substrate, we could cover those CNTs not expected to be cut off by the Polydimethylsiloxane (PDMS) films under the assistance of numeric markers (Supplementary Figure 9), so that the specific ultralong CNTs could be cut off using the above method. After the two ends being cut off, the ultralong CNT between these ends will become a nanochannel for measuring water transport. Thus, we can produce nanochannels of definite length by controlling the distance between the two cut-off points.

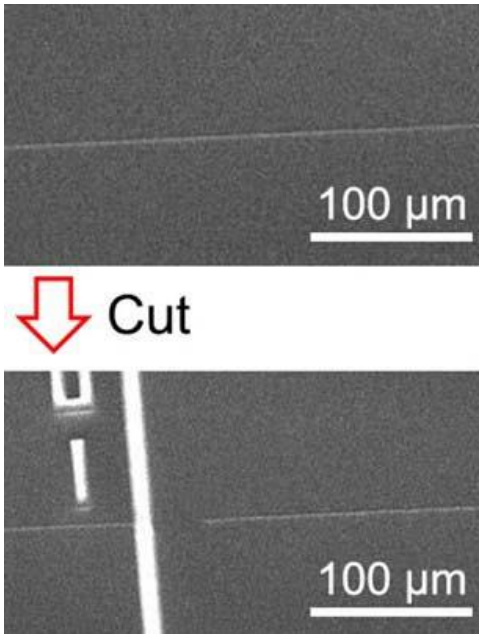

Supplementary Figure 8. The SEM images of the same ultralong CNT before and after being cut.

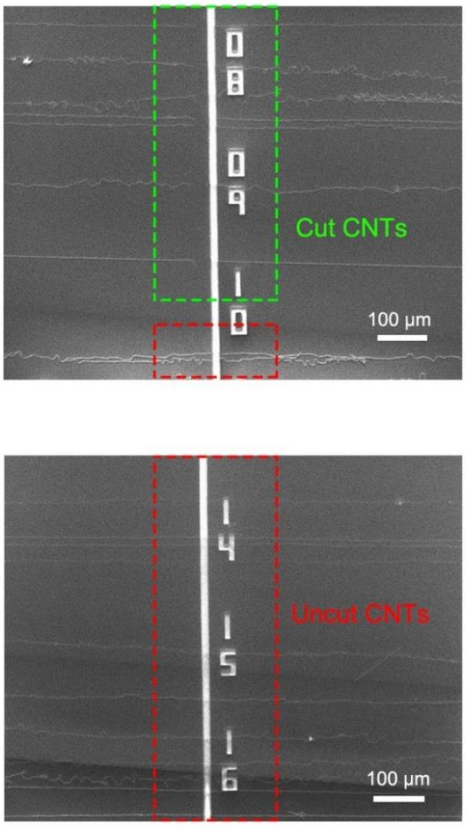

Supplementary Figure 9. The SEM images showing the CNTs cutting at the same x position on the substrate. We used the probe to cut the CNTs in upper area (marked by 08, 09 and 10), while the CNTs in lower area (marked by 14, 15 and 16) are uncut. The efficiency of CNT cutting is confirmed by comparing these two images.

Supplementary Discussion 5

Generally, a mass spectrometer is mainly composed of four parts: sampling system, ion source, mass analyzer and detector. As shown in the Supplementary Figure 10, the gas enters the flange through the capillary from the entrance and is divided into two branches. One branch of gas enters the vacuum chamber through the orifice, and then is ionized and detected. The other one does not enter the vacuum chamber, but is directly pumped into the pump group through a thicker pipe. Apparently, such a sampling system is only suitable for measuring a large amount of gas.

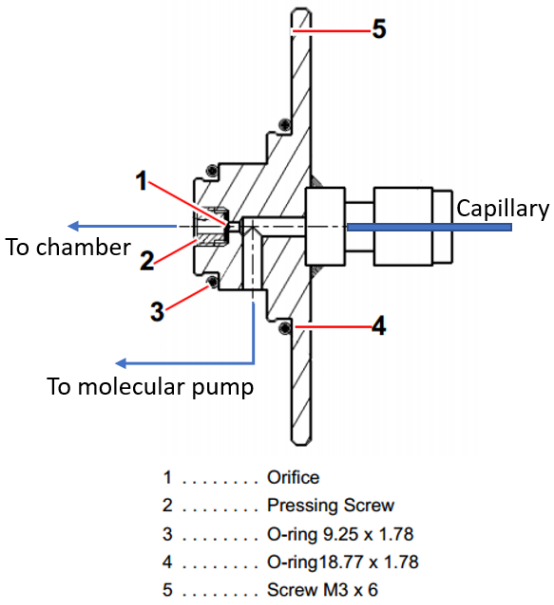

Supplementary Figure 10. The sectional profile of the sampling system of the mass spectrometer.

The mass flow rate of water through a CNT can be as low as subpicogram to femtogram per second, which will be detected mostly in the form of noise, because a large amount of gas will be directly taken away from the pump group. Therefore, we have modified the mass spectrometer by removing the pump group, so that water passing through the CNT will all enter the vacuum chamber. Meanwhile, some components leading to high pressure drop were also removed, such as orifice, capillary, throttle valve, *etc*., to reduce the flow resistance and pressure drop of the channel, as well as the residence time of water in the channel. And the ultralong CNT channel was directly connected with the flange of the sampling system as shown in Figure 1e. Because of these modifications, the sampling system was directly connected with the vacuum chamber under low flow resistance and low pressure drop, ensuring that all the materials entering the sampling system were pumped into the vacuum chamber for detection. Thus, it successfully paves a way towards transport measurement in an individual ultralong CNT.

The ultralong CNT can be regarded as a pipe with a nanoscale diameter. The sealing of the set-up should ensure that the nanotube is the only channel connecting the

atmospheric end with the sampling system of mass spectrometer. This sealing configuration can be divided into the axial part and radial part.

In the radial part, the pressure generated by the clamp-cuff will squeeze the O-ring to achieve sealing. In order to prevent the sealant from being compressed and deformed which might destroy axial tightness or even the microstructure of CNT, a stainless stent was added within the rubble O-ring (Supplementary Figure 11b). And the sealant was used to bond the Si/SiO_2 substrate (loaded with grown ultralong CNTs) with the stainless stent. It could achieve better sealing, which was also easier for disassembly.

In the axial part, Agilent Torr Seal, a high-performance vacuum epoxy resin A-B adhesive, was used for sealing. The sealing with the adhesive was realized by solidifying a mixture of liquid resin and curing agent in a ratio of 2:1. Due to its ultralow vapor pressure, it could be used to seal high-vacuum systems. After being mixed, it was placed at room temperature for about 24 to 48 hours, and after complete solidification, could be further used.

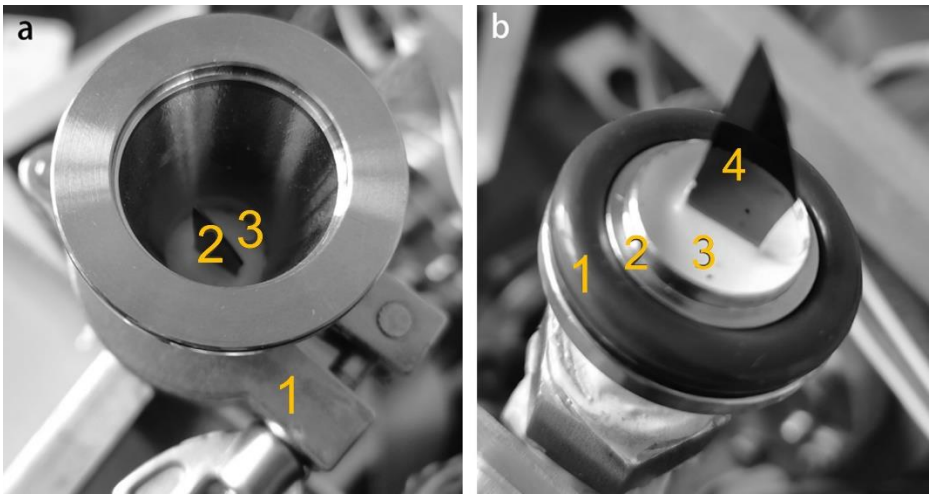

Supplementary Figure 11. Sealing of the set-up for transport experiment through an ultralong CNT. (**a**) Sealing state. 1, clamp; 2, Substrate loaded with CNTs; 3, Ultrahigh vacuum epoxy resin. (**b**) Opening state. 1, O-ring; 2, Stainless steel stent; 3, Ultrahigh vacuum epoxy resin; 4, Substrate loaded with CNTs.

Supplementary Discussion 6

Assume that H_2O flows through the ultralong CNT at a flux of 1×10^{-13}g/s, all of which enters the vacuum chamber of the mass spectrometer. The volume V, of the vacuum chamber is 2 L, and the room temperature T is 298 K. The ideal gas equation of state can be applied for the high-vacuum system, and the maximum pressure change per second caused by the flow entering the vacuum chamber can be described as below.

$$\Delta P = \frac{\Delta nRT}{V} = \frac{\Delta mRT}{MV} = 6.88 \times 10^{-9}\ Pa/s \qquad (S1)$$

where M is the molar mass of H_2O, and R is the ideal gas constant. The pressure change can be directly detected within the detection limit of the mass spectrometer system, namely 2×10^{-11} Pa.

Besides, the total pressure in the vacuum chamber is about 10^{-5} Pa, where the partial pressure of H_2O is nearly 10^{-6} Pa. If H_2O was selected as the measurement medium, because of its large background signal, such a small pressure change (only about one thousandth of the partial pressure per second) would be easily submerged in the background fluctuation. Therefore, D_2O was used as the measurement medium, and the mass spectrometer was used to measure the ion current intensity corresponding to D_2O molecules (m/z=20). It is because the natural abundance of D_2O is about 0.02 %, whose background signal is low in the mass spectrometer. And the pressure change as low as 10^{-9} Pa/s can be sensitively detected when D_2O flows through the CNT. Moreover, D_2O possess similar physicochemical properties to H_2O, which will have no influence on the super-transport analysis. As shown in Supplementary Figure 12, repeated changes of the partial pressure of D_2O can be seen, and the transport behaviors are similar when either D_2O or H_2O flows through the ultralong CNT.

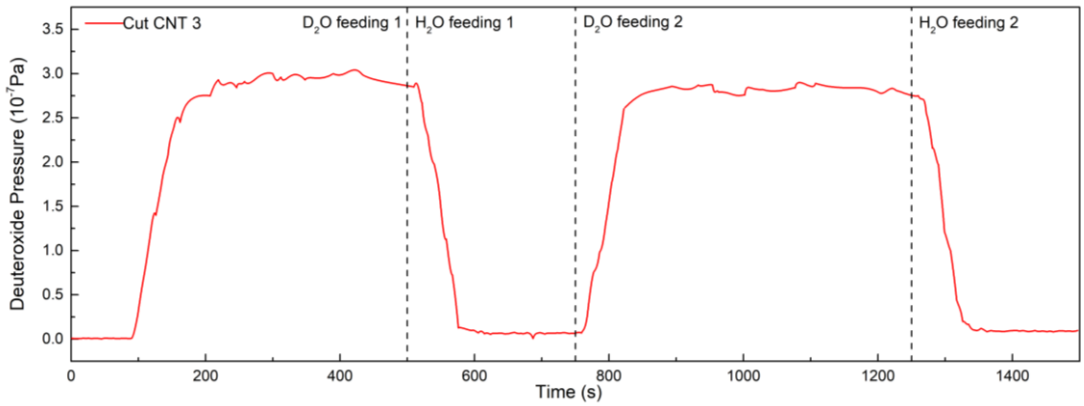

Supplementary Figure 12. Recyclable pressure changes of D_2O when the transport medium continuously switches between D_2O and H_2O.

Supplementary Discussion 7

As shown in the Figure 2a, during the filling and transport processes, there were two stages of signal change. In the first stage, there was no detectable change for both air and D_2O. In the second stage, the measured air and D_2O signals began to change synchronously. And the pressure of the initial media (air in the filling process, D_2O in the transport process) together with the newly filled media (D_2O in the filling process, H_2O in the transport process) in the vacuum chamber exponentially changed at the same time. As indicated by such synchronization, the transport through the CNT is characteristic of plug flow, media transporting through the nanotube will not mix with each other. And there is uniform velocity distribution along the radial direction of the nanotube. While in the vacuum chamber, they have exhibited the ideal characteristics of "complete mixing flow". It indicates that the transport media in the CNT can be detected by the mass spectrometer immediately after leaving the orifice towards the chamber.

Since the partial pressure signals measured by mass spectrometer are a series of discrete points, rather than continuous signals, there will be a time difference until a signal response is generated. As a result, the time at which the partial pressure signal begins to change is not necessarily the time when the transport media actually enters the vacuum chamber. According to the transport mode of plug flow-complete mixing flow, the time consumed by the plug flow in the nanotube is the delay time of the signal change in the vacuum chamber after changing the transport media. Therefore, the transport velocity in CNT can be calculated by:

$$v = \frac{L}{\Delta t} \tag{S2}$$

where L is the length of a single ultralong CNT, Δt is the delay time from the change of the transport media at the entrance to the response of D_2O in the mass spectrometer. This equation can be used for both the filling and transport process.

On the other hand, the behavior of the media mixed in the vacuum chamber exhibits the characteristics of "complete mixing flow". Therefore, when the flux entering the vacuum chamber changes abruptly, the corresponding partial pressure signal will change exponentially as below:

$$P = P_0 + A \cdot e^{-\frac{t-t_0}{\tau}} \tag{S3}$$

where P_0 is the partial pressure of D_2O at equilibrium state, and A and t_0 are constants. τ is the residence time in the vacuum chamber, which is also a constant. During the filing process of D_2O, the flow entering the vacuum chamber increases, and the partial pressure of D_2O increases, so that A is negative. And during the transport process of H_2O, the D_2O flux entering the vacuum chamber decreases and the partial pressure of D_2O decreases, so that A is positive.

By fitting the signal curve after the abrupt change of partial pressure, the above four

constant values can be calculated. Then let $P = P_{ini}$, where P_{ini} is the partial pressure of D_2O before the signal change. Thus, the value of t can be obtained, corresponding to the time when the transport media actually enters the vacuum chamber. After subtracting this t value with the time when changing the transport media in the atmosphere, the accurate delay time Δt can be calculated.

Supplementary Discussion 8

As a benchmark, we connected the same ultralong CNT before and after being cut, to the sampling system of the mass spectrometer respectively, so as to compare their different water transport processes. It can be seen from Supplementary Figure 13 that signals can only be measured in the ultralong CNT which is cut, and the signals of uncut CNT before and after water immersion do not change significantly. It indicates that the measured signals of D_2O come from the "cutting" operation. In other words, all the measured signals of D_2O are derived from the transport process inside the ultralong CNT. It proves that when the end of CNT in the atmosphere is immersed in D_2O, our well-sealed setup does not lead to any leakage which can be detected by the mass spectrometer.

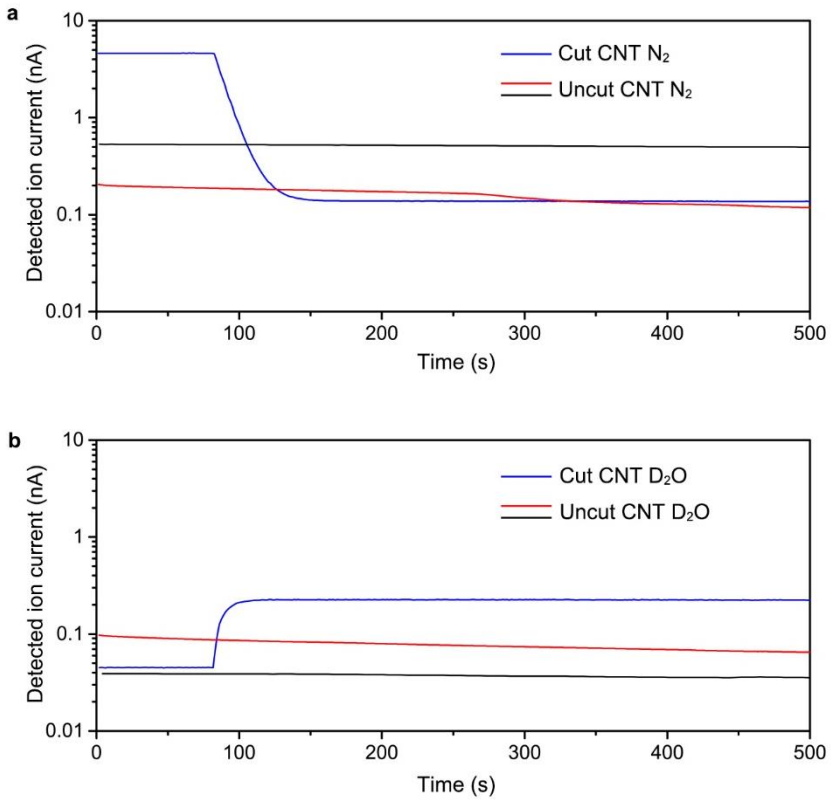

Supplementary Figure 13. Partial pressure changes of D_2O detected in the mass spectrometer through the same ultralong CNT before and after being cut.

Supplementary Discussion 9

The modified slippage Hagen-Poiseuille (MSHP) model was established to uniformly understand the results in this work and previous studies. The MSHP model includes both the slippage and entrance/exit losses, where the pressure drop ΔP takes the form:

$$\frac{\Delta P}{v} = \frac{8\mu L}{R^2 + 4RL_s} + \frac{\pi\mu C}{R} \tag{S4}$$

where two terms represent the contributions of slippage (first) and entrance/exit effect (second), respectively, and the coefficient C represents the sum of entrance/exit losses (as shown in Supplementary Figure 14). The enhancement ratio is calculated by $\varepsilon = v/v_{HP}$ to get Eq. 6. Even for the ultralong CNT in this work, the losses at entrance and exit may dominate the total losses, and the first term in Eq. 6 can be ignored so that the ε and the aspect ratio L/R of CNTs are nearly in proportion.

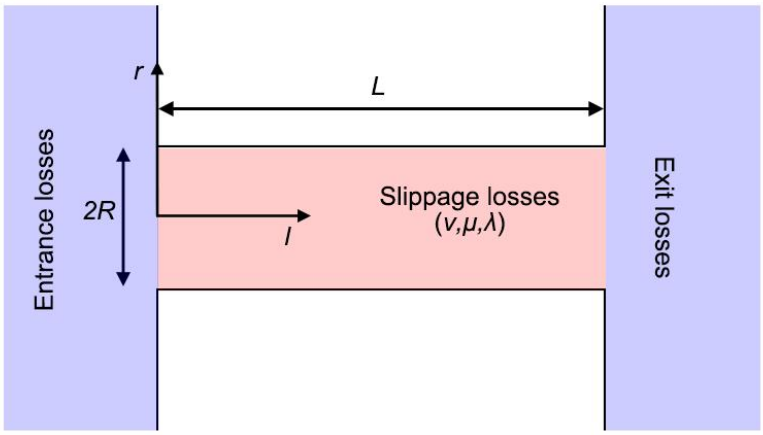

Supplementary Figure 14. Schematic diagram for the MHP models.

To explain the relation between λ and L in Fig. 4a, we take the assumption into Eq. 2 and Eq. 6 that the entrance/exit effect is dominant for those short CNTs in previous works. First, because the λ is low enough, Eq. 2 can be simplified as:

$$v = \frac{\Delta P(R^2 + 4R\frac{\mu}{\lambda})}{8\mu L} \approx \frac{\Delta PR}{2L\lambda} \tag{S5}$$

Substitute it into Eq. S4 and ignore the first term in Eq. S4 (as we mentioned above, it can be ignored for the short CNTs):

$$\frac{\Delta PR}{2L\lambda} \approx \frac{\Delta PR}{\pi\mu C} \tag{S6}$$

Then, we can get an inversely proportional relation between λ and L as $\lambda \approx \pi\mu C/(2L)$.

Supplementary Discussion 10

As shown in Supplementary Figure 15, it is a graphical expression of the SHP model revealing the correlation among viscosity μ, friction coefficient λ and water flow rate Q_{SHP}. It can be seen that within a wide range of viscosity (10^{-8}~10^{-3} Pa·s), the flow rate is not associated with viscosity but only with the friction coefficient.

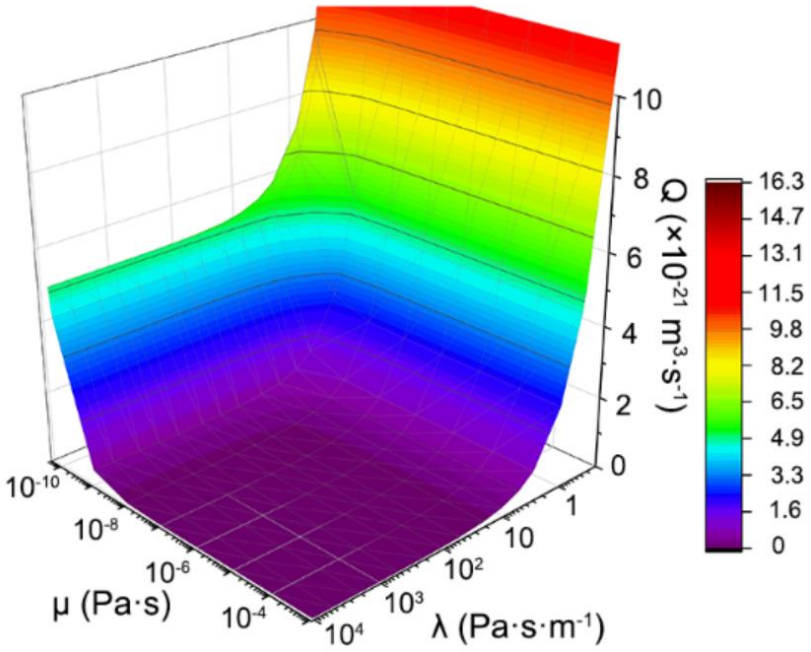

Supplementary Figure 15. Correlation among Q_{SHP}, μ and λ, where the change in viscosity μ from 10^{-8} to 10^{-3} Pa·s will not affect the water flow rate Q_{SHP} (that is, the velocity v).

Supplementary Table

Experimental process of measuring the water transport through an ultralong CNT.

Time	Event
0	The end of CNT exposed to air is immersed in deuteroxide, and the filling process of deuteroxide begins in the CNT.
t_1	The CNT is completely filled with deuteroxide, and deuteroxide begins to enter the vacuum chamber. The partial pressure of deuteroxide in the vacuum chamber begins to rise.
t_2	The flux of deuteroxide in the vacuum chamber reaches equilibrium. The measured partial pressure of deuteroxide in the vacuum chamber reaches a stable value.
t_3	Remove the deuteroxide from the air end of the CNT and replace it with deionized water. The transport process of deionized water being replaced by deuteroxide begins in the CNT.
t_4	The CNT is completely filled with deionized water, and deionized water begins to enter the vacuum chamber. The partial pressure of deuteroxide in the vacuum chamber begins to decrease.
t_5	The deuteroxide in the vacuum chamber reaches equilibrium again. The measured partial pressure of deuteroxide in the vacuum chamber reaches a stable value.
t_6	The deionized water at the air end can be replaced by deuteroxide to continue the experiment.

Supplementary References

44 Dresselhaus, M. S., Jorio, A., Hofmann, M., Dresselhaus, G. & Saito, R. Perspectives on Carbon Nanotubes and Graphene Raman Spectroscopy. *Nano Lett.* **10**, 751-758 (2010).

45 Dresselhaus, M. S., Dresselhaus, G., Saito, R. & Jorio, A. Raman spectroscopy of carbon nanotubes. *Phys. Rep.* **409**, 47-99 (2005).

46 Dresselhaus, M. S., Dresselhaus, G., Jorio, A., Souza Filho, A. G. & Saito, R. Raman spectroscopy on isolated single wall carbon nanotubes. *Carbon* **40**, 2043-2061 (2002).

47 Wu, W. *et al.* True-color real-time imaging and spectroscopy of carbon nanotubes on substrates using enhanced Rayleigh scattering. *Nano Res.* **8**, 2721-2732 (2015).

48 Liu, K. *et al.* High-throughput optical imaging and spectroscopy of individual carbon nanotubes in devices. *Nat. Nanotechnol.* **8**, 917-922 (2013).

49 Sfeir, M. Y. *et al.* Optical Spectroscopy of Individual Single-Walled Carbon Nanotubes of Defined Chiral Structure. *Science* **312**, 554-556 (2006).

50 Sfeir, M. Y. *et al.* Probing Electronic Transitions in Individual Carbon Nanotubes by Rayleigh Scattering. *Science* **306**, 1540-1543 (2004).

51 Liu, K. *et al.* Quantum-coupled radial-breathing oscillations in double-walled carbon nanotubes. *Nat. Commun.* **4**, 1375 (2013).

52 Liu, K. *et al.* An atlas of carbon nanotube optical transitions. *Nat. Nanotechnol.* **7**, 325-329 (2012).

53 Liu, K. *et al.* Van der Waals-coupled electronic states in incommensurate double-walled carbon nanotubes. *Nat. Phys.* **10**, 737-742 (2014).

54 Wen, Q. *et al.* 100 mm Long, Semiconducting Triple-Walled Carbon Nanotubes. *Adv. Mater.* **22**, 1867-1871 (2010).

55 Huang, S., Woodson, M., Smalley, R. & Liu, J. Growth Mechanism of Oriented Long Single Walled Carbon Nanotubes Using “Fast-Heating” Chemical Vapor Deposition Process. *Nano Lett.* **4**, 1025-1028 (2004).